INTERNATIONAL JOURNAL FOR NUMERICAL METHODS IN FLUIDS
*Int. J. Numer. Meth. Fluids* 2006; **51**:1419–1438
Published online 10 February 2006 in Wiley InterScience (www.interscience.wiley.com). DOI: 10.1002/fld.1181

# Stability of Navier–Stokes discretizations on collocated meshes of high anisotropy and the performance of algebraic multigrid solvers

R. Webster*,†

*Roadside, Harpsdale, Halkirk, Caithness, KW12 6UL, Scotland, U.K.*

SUMMARY

A numerical instability is identified in Navier–Stokes discretizations on meshes of high anisotropy. The instability occurs under conditions of low Reynolds number (and in the Stokes limit) for collocated-mesh discretizations based on physical (momentum) interpolation schemes. It is responsible for the poor performance reported for some algebraic multigrid solvers (previously attributed to possible deficiencies in the solvers).

The problem may be alleviated by not employing uniformly anisotropic meshes. A graded stretching/compaction that leaves part of the domain spanned by elements of moderate aspect ratio can provide sufficient velocity–pressure coupling to stabilize the system. Copyright © 2006 John Wiley & Sons, Ltd.

KEY WORDS: Navier–Stokes; physical interpolation; fully coupled solutions; algebraic multigrid

## 1. INTRODUCTION

In a previous series of papers [1–4], an algebraic multigrid (AMG) solver was presented for application in the solution of Navier–Stokes problems. This provided coupled solutions for fluid flow and pressure, for the linear approximations associated with each Picard iteration of a non-linear solver. As it was a fully coupled method, no under-relaxation of the flow variables was necessary to assist convergence. The AMG method was based on zero-order inter-grid transfer operators, so the algorithm was simple and efficient in terms of storage requirements and operation count, which of course it needed to be if it was to be used repeatedly for Picard iterations. However, zero-order transfer operators were not entirely satisfactory for the second-order, elliptic aspects of the Navier–Stokes equations: At least first-order restriction/interpolation should strictly have been used to ensure a consistent coarse grid approximation (CGA), and hence a full-bandwidth correction spectrum. To improve the CGA, a simple scaling scheme was adopted which did not compromise either the storage

*Correspondence to: R. Webster, Roadside, Harpsdale, Halkirk, Caithness, KW12 6UL, Scotland, U.K.
† E-mail: ronniewebster@aol.com

*Received 23 September 2005*
*Revised 22 November 2005*
*Accepted 26 December 2005*

requirements or the operation count. However, there remained the question as to whether this simplified approach would be sufficiently effective and robust when compared with the alternative, but more costly, approach of using higher-order inter-grid transfer operators.

In the most recent paper [4], therefore, a comparison was made of the two methods, AMG0 and AMG1; AMG0 based on zero-order operators (with CGA scaling), AMG1 based on first-order operators (both restriction and prolongation). The comparison focussed on low-Reynolds-number flows (i.e. $Re<1$), a hard test for AMG0 (an easy test for AMG1). Higher Reynolds number flows ($1\leqslant Re\leqslant 3200$) had been the subject of the earlier papers [1–3]. The investigation also considered highly anisotropic grids that are often employed in Navier–Stokes discretizations. Other elliptic problems were also addressed including pure diffusion, elastic strain fields in solids as well as inherently discrete network problems. It was found that AMG0 performed well on all problems except for viscous flow on uniform meshes assembled using, exclusively, elements of extreme aspect ratio where, somewhat surprisingly, both AMG0 and AMG1 could sometimes fail, whereas neither failed for similarly distorted meshes in the other applications. It was suggested that more complex smoothers might be required for such coupled-field applications, of the kind used in geometric multigrid algorithms.

It is the purpose of the present paper to show by a combination of analysis and numerical experiment, that the root cause of the problems encountered is a potentially unstable Navier–Stokes discretization, due to a weakening of velocity–pressure coupling on highly anisotropic meshes. To avoid the problem, without changing the existing element interpolation scheme and without large investments in smoothing, it is necessary to avoid the homogeneous deployment of large-aspect-ratio elements across the entire calculational domain.

## 2. DISCRETIZATION

### 2.1. Notation

Discrete variables will be represented by algebraic vectors which will be written in bold face characters, e.g. $\mathbf{x}$, or alternatively in the form $x(j)$, where index $j$ could be a nodal index, field index, an element face/edge/vertex index, etc. Physical vectors will also be denoted either by bold face letters, e.g. $\mathbf{x}$, or alternatively by tensor notation, e.g. $x_i$, where the subscript identifies the vector component. Where the entries in, $x(j)$, are themselves a physical vector then $\mathbf{x}(j)$ or $x_i(j)$ will be used to emphasize this. To distinguish interpolation point variables within elements from their nodal counterparts, a superscript will be used, e.g. $\mathbf{x}^e$. The equivalent system variable (for all elements) would then be written $\mathbf{x}^e(e)$, where the integer variable, $e$, is an element index. The $x, y$ notation is used for two-dimensional Cartesian co-ordinates.

### 2.2. Discrete equation system

The calculational domain is subdivided into a large assembly of finite elements (in this case triangular). The discrete flow variables of velocity, $\mathbf{u}(j)$, and pressure, $p(j)$, are collocated at nodes placed at element vertices. The element assembly may be unstructured, so the density of elements can vary within the domain. The elements are designated to have a volume, $V^e$. Element edges/faces are designated to have an area, $\mathbf{A}(j)$ (Figure 1). The medians cut elements from the centroid to face centres into three equal segments. Assigning each segment to its vertex node forms a complete set of nodal control volumes, the median dual cells

 

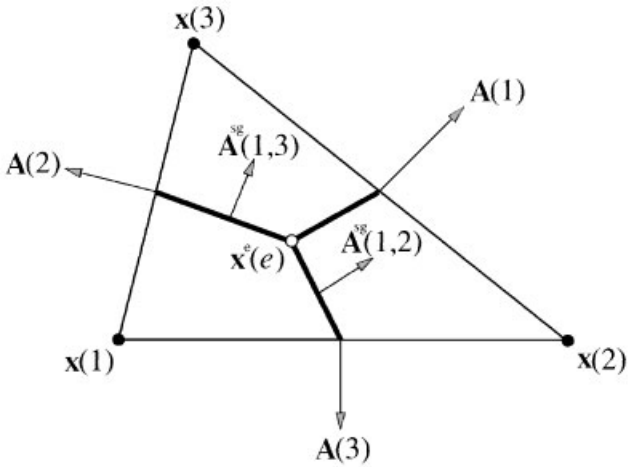


Figure 1. Triangular element; face area vectors $\mathbf{A}(i)$; nodal variables ($\mathbf{x}(i)$); element variables ($\mathbf{x}^e(e)$) and segment surfaces $A^{sg}(i,j) = [\mathbf{A}(i) - \mathbf{A}(j)]/6$.

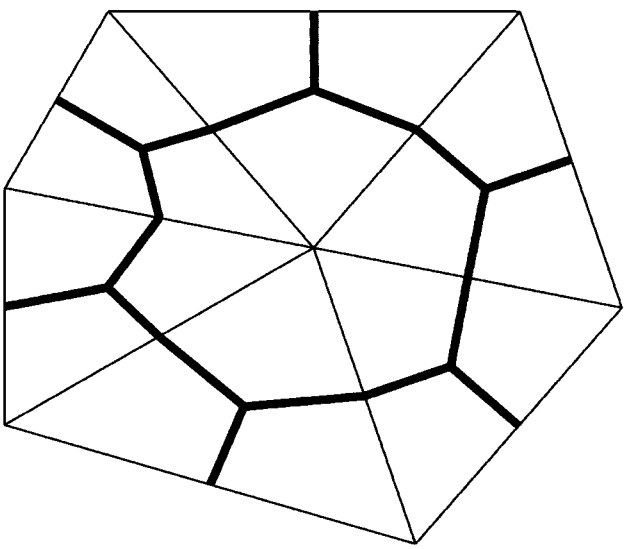

Figure 2. Six triangular elements and seven median dual cell control volumes.

(Figure 2). Enforcement of the conservation laws for fluid flow consistently for every such nodal control volume delivers the discrete Navier–Stokes equation set for the system. Thus, for an incompressible fluid, enforcement of momentum and mass conservation, respectively, gives the following coupled system:

$$\mathbf{Q}(\mathbf{u})\mathbf{u} + \mathbf{\Gamma}\mathbf{p} = \mathbf{s} \tag{1a}$$

$$\mathbf{\Gamma}^*\mathbf{u} = 0 \tag{1b}$$

 

where $\mathbf{Q}(\mathbf{u})$ is the discrete advection–diffusion matrix operator, a function the nodal velocity, $\mathbf{u}$; $\mathbf{\Gamma}$ is the discrete nodal gradient operator; $\mathbf{\Gamma}^*$ is the discrete nodal divergence operator; $\mathbf{s}$ and $\mathbf{s}^m$ represent the respective volumetric sources. The absence of pressure in (1b) precludes the use of normal relaxation methods in solving this system iteratively. Methods such as ILU factorization or the distributive iteration methods such as that of Brandt and Dinar [5] could be used, but there are other problems with the system as it stands. Simple linear interpolation on collocated meshes renders it unstable [6]. This arises because the velocity at any particular node does not depend on the pressure at that node but only on pressure differences between its adjacent neighbours, i.e. no diagonal entry in $\mathbf{\Gamma}$. Similarly, any flow imbalance for a particular nodal control volume does not depend on the velocity at the associated node, but only on velocity differences between neighbouring nodes, i.e. no diagonal entry in $\mathbf{\Gamma}^*$. These insensitivities allow chequer-board types of spatial instability. For example if $\mathbf{M}$ is an easily inverted part of $\mathbf{Q}$, and a splitting $\mathbf{Q}=\mathbf{M}+\mathbf{N}$ were used to derive a pressure equation from (1a) and (1b), i.e.

$$(\mathbf{\Gamma}^*\mathbf{M}^{-1}\mathbf{N})\mathbf{u}+(\mathbf{\Gamma}^*\mathbf{M}^{-1}\mathbf{\Gamma})\mathbf{p}=\mathbf{s}' \tag{1c}$$

where $\mathbf{s}'=\mathbf{\Gamma}^*\mathbf{M}^{-1}\mathbf{s}-\mathbf{s}^m$, then there will be no adjacent-neighbour couplings in the pressure matrix $(\mathbf{\Gamma}^*\mathbf{M}^{-1}\mathbf{\Gamma})$; instead, it will take the form of two spatially separated, decoupled, sub-systems each consisting of next-nearest neighbours in checker-board pattern. It was this problem which led to the development of the long established staggered-grid method of Harlow and Welch (see, for example, Reference [6]).

However, the inconvenience of staggered meshes for local refinement and for problems with so-called complex geometry, has spurred the development of various alternative interpolation schemes that provide the required velocity–pressure coupling to stabilize discretizations for collocated meshes. Early schemes were the so-called momentum interpolation schemes, somewhat similar to that originally devised by Rhie and Chow [7]. More physically consistent schemes were devised by Prakash [8], Hookey [9] and by Schneider and Raw [10]. Derivatives of the Schneider and Raw approach are, the scheme used here [1–4] and the consistent physical interpolation (CPI) scheme of Deng *et al.* [11]. The interpolated velocities in the schemes not only depend on the local nodal velocities, but also on the local nodal pressures (as well as on any sources or sinks within the element). For the triangular elements used here just one interpolation point at each element centroid, index $e$, for a single flow velocity, $\mathbf{u}^e(e)$, is used for calculating fluxes within the element. The derivation of the interpolation is described below. Replacing (1b) with the divergence of the element velocities and replacing $\mathbf{u}^e(e)$ by the interpolation functions (see Section 2.3 below), transforms the system to

$$\mathbf{Q}(\mathbf{u}^e)\mathbf{u}+\mathbf{\Gamma}\mathbf{p}=\mathbf{s} \tag{2a}$$

$$\mathbf{C}\mathbf{u}+\mathbf{B}\mathbf{p}=\mathbf{s}^p \tag{2b}$$

where $\mathbf{C}$ is another form of discrete divergence operator, $\mathbf{s}^p$ is a modified source, and matrix $\mathbf{B}$, unlike $(\mathbf{\Gamma}^*\mathbf{Q}^{-1}\mathbf{\Gamma})$, is a Poisson-type operator with adjacent-neighbour couplings. These derive directly from the $\mathbf{u}$–$p$ coupling of the interpolation and are directly responsible for stabilizing the system. The form of $\mathbf{B}$ also enables the system to be solved iteratively using normal relaxation methods.

 

### 2.3. *Element interpolation*

A pointer to the source of the convergence problems in the previous work lay in the observation that none were encountered for other elliptic problems on similarly stretched meshes. It was only for the Navier–Stokes applications that both AMG0 and AMG1 encountered difficulties. For example, for a scalar diffusion problem on a uniform mesh of elements of aspect ratio $\alpha = 256$, a residual-reduction factor $\rho = \mathbf{r}^i/\mathbf{r}^{i-1} \sim 10^{-7}$ was achieved using AMG0 with an ILU smoother ($\mathbf{r}^{i-1}$ and $\mathbf{r}^i$ being the residuals in successive iterations, $i-1$ and $i$). Convergence to machine accuracy could be achieved in just two multigrid F-cycles, the smoother acting almost like a TDMA direct solver for high aspect ratio discretizations, whereas the same solver and smoother failed ($\rho \approx 1$) when applied to the Navier–Stokes problem for the same mesh. This prompted a re-examination of the above-mentioned interpolation used within elements.

For the present, attention will be focussed on a single element. The derivation of the interpolation equation uses a second enforcement of the conservation laws applied to a sub-control volume constructed within the element. This gives the element velocity, $\mathbf{u}^e(e)$, as a function both of the vertex nodal velocities, $\mathbf{u}(j)$, and the vertex nodal pressures, $p(j)$, as well as on any volumetric sources or sinks of momentum internal to the element, $\mathbf{s}(e)$. A six sided control cell is constructed by joining the mid-points of sides to the mid-points of median lines joining the centroid to the vertices (Figure 3). This gives the six surfaces, $\pm \boldsymbol{A}^s(i)$, where

$$\pm \boldsymbol{A}^s(i) = \pm \mathbf{A}^{sg}(j,k) = \frac{\pm(\mathbf{A}(j) - \mathbf{A}(k))}{6}$$

with a cyclic permutation of $i$, $j$, $k$, two surfaces for each of the three vertex segments. Finite-volume approximations for velocity gradients in each segment, $\nabla u_i(l)$, can be calculated where

$$\nabla u_i(l) = \frac{3(\mathbf{A}(l)[u_i^e(e) - u_i(l)] - 2\boldsymbol{A}^s(l)[u_i(m) - u_i(n)])}{4V^e}$$

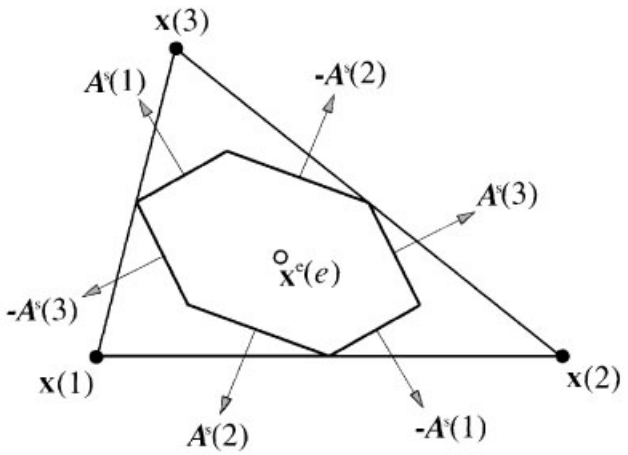


Figure 3. Element sub-control volume, bounded by control surfaces $\mathbf{A}^s(l) = \pm[\mathbf{A}(m) - \mathbf{A}(n)]/6$ (cyclic permutation of $l$, $m$, $n$).

 

with again cyclic permutation of $l$, $m$, $n$. Thus, if $\mu$ is the fluid viscosity, a net diffusive flux component of momentum may be calculated for the control surfaces in each segment

$$\mathbf{F}_i(l) = -\mu \nabla u_i(l) \left( \frac{2[\boldsymbol{A}^s(m) - \boldsymbol{A}^s(n)]}{V^e} \right)$$

Substituting for $\nabla u_i(l)$ and for $\boldsymbol{A}^s(l)$, $\boldsymbol{A}^s(m)$, $\boldsymbol{A}^s(n)$ and summing the fluxes for all three segments gives a net diffusive flux, $F_i^D(e)$, for the element sub-control volume

$$F_i^D(e) = \mu \left[ 3u_i^e(e) - \sum_{r=1}^{3} u_i(r) \right] \sum_{q=1}^{3} \left\{ \frac{A_i(q) A_i(q)}{(2V^e)^2} \right\}$$

with the summation convention for repeated physical vector/tensor subscripts understood. Moreover, since $A_i(q)A_i(q) = |A(q)|^2$ and $2V^e/|A(q)| = \Delta(q)$, the perpendicular height of the vertex $q$, the net diffusive flux may be re-written as

$$F_i^D(e) = \mu \left[ 3u_i^e(e) - \sum_{r=1}^{3} u_i(r) \right] \sum_{q=1}^{3} \left\{ \frac{1}{\Delta^2(q)} \right\} \tag{3}$$

A similar accountancy can be performed for the advective fluxes. To this end upwind advective flux velocities, $u^{\pm}(e,q)$, are defined for the net control surface direction, $\mathbf{a}(q)$, in each segment where

$$u^{\pm}(e,q) = \frac{[u_j^e(e) a_j(q) \pm |u_j^e(e) a_j(q)|]}{2}$$

and $\mathbf{a}(q) = -\mathbf{A}(q)/|\mathbf{A}(q)|$. Thus, the upstream momentum flux components advected in/out of the sub-control volume will be

$$F_i^A(e) = \rho \sum_{q=1}^{3} \left\{ \frac{[u^-(e,q) u_j(q) + u^+(e,q) u_i^e(e)]}{\Delta(q)} \right\} \tag{4}$$

Momentum flux due to the body force associated with pressure differences, $F_i^B(e)$, may similarly be calculated,

$$F_i^B(e) = \sum_{q=1}^{3} \left\{ \frac{a_i(q) p(q)}{\Delta(q)} \right\} \tag{5}$$

The sum of these fluxes must balance any sources or sinks, $s_i(e)$, within the element

$$F_i^A + F_i^B + F_i^D = s_i(e) \tag{6}$$

Substituting (3)–(5) into (6), adopting a linearized approximation for the advection terms, defining an advection coefficient, $\mathrm{K}^{\pm}(q)$, a diffusion coefficient, $D$, an element–segment gradient operator, $g_i(q)$, element–segment Peclet numbers, $Pe^{\pm}(q)$, and an element Peclet number, $Pe^{+}$ where

$$K^{\pm}(q) = \frac{\rho u^{\pm}(e,q)}{\Delta(q)}, \quad D = \mu \sum_{q=1}^{3} \frac{1}{\Delta^2(q)}, \quad g_i(q) = -\frac{a_i(q)}{\Delta(q)}$$

 

$$Pe^{\pm}(q) = \frac{K^{\pm}(q)}{D} \quad \text{and} \quad Pe^{+} = \sum_{q=1}^{3} Pe^{+}(q)$$

and, re-arranging, the following equation can be constructed:

$$Q_{ii}^{e} u_i^{e}(e) = s_i^{e}(e) + \sum_{r=1}^{3} \{[1 - Pe^{-}(r)]u_i(r)\} + \sum_{q=1}^{3} \{g_i(q)\, p(q)\}$$

where $Q_{ii}^{e} = D(3 + Pe^{+})$, with $Q^{e}$ an advection–diffusion, matrix for the element (diagonal in this inertial frame). The interpolation equation is thus

$$u_i^{e}(e) = C^{s} s_i^{e}(e) + \sum_{q=1}^{3} \{C^{V}(q) u_i(q)\} + \sum_{q=1}^{3} \{C_i^{p}(q)\, p(q)\} \tag{7}$$

and the interpolation coefficients, relating, $u_i^{e}(e)$, to the sources/sinks, $s_i^{e}(e)$, and to the nodal velocities and pressures, $u_i(q)$ and $p(q)$, are therefore

$$C^{s} = [Q_{ii}^{e}]^{-1} = \frac{1}{D(3 + Pe^{+})}, \quad C^{V}(q) = \frac{[1 + Pe^{-}(q)]}{(3 + Pe^{+})}, \quad C_i^{p}(q) = [Q_{ii}^{e}]^{-1} g_i(q)$$

Of particular importance, therefore, in determining the strength of the **u**–**s** and the **u**–$p$ coupling and hence the stability of the discretization, are the element Peclet numbers and the inverse of the element advection–diffusion operator, $[Q_{ii}^{e}]^{-1}$.

First, consider low Peclet numbers due to low velocity, $Pe^{\pm} \to 0$ as $\mathbf{u} \to 0$. The **u**–$p$ coupling coefficient, $C_i^{p}(q)$, remains finite, since $[Q_{ii}^{e}]^{-1} \to (3D)^{-1}$ as $Pe^{\pm} \to 0$ and there is no breakdown in coupling. Next, consider low Peclet numbers caused by a large diffusivity, $Pe^{\pm} \to 0$ as $D^{-1} \to 0$. Now there is a breakdown, $[Q_{ii}^{e}]^{-1} \to 0$ as $D^{-1} \to 0$, $C^{s} \to 0$, $C_i^{p}(q) \to 0$, $C^{V}(q) \to 1/3$, giving a simple linear interpolation, which is known to be unstable.

So the diffusion coefficient, which is a flow resistivity coefficient for the element, is the important factor. The higher the resistivity the weaker the coupling and the less stable the system (which is counter to the stabilizing influence which is normally expected from a resistivity). Now,

$$D^{-1} = \mu \sum_{q=1}^{3} \left\{ \frac{1}{\Delta^{2}(q)} \right\}^{-1} = \frac{\delta^{2}}{3\mu}$$

where the harmonic mean height of the vertices, $\delta$, is naturally biased towards the shortest height. Thus, the smaller the element, and the more viscous the fluid, the weaker the **u**–$p$ coupling and therefore the less stable the system. For a given fluid viscosity, moreover, the element need only be small in one dimension in order to have a relatively high diffusivity. This is because of the relatively large area for the transverse diffusion of momentum when an element has a small height-to-length ratio (i.e. high aspect ratio). This situation is of course precisely that for which the convergence problems were encountered in Reference [4].

### *2.4. The pressure equation*

Consider now the pressure equation, obtained by enforcing continuity. Extending (7) to all elements gives

$$\mathbf{u}^{e} = [\mathbf{Q}^{e}]^{-1} \mathbf{s}^{e} + \mathbf{C}^{V} \mathbf{u} + [\mathbf{Q}^{e}]^{-1} \mathbf{G} \mathbf{p}$$

 

$\mathbf{Q}^e$ being the diagonal, $N^e \times N^e$, block-diagonal advection–diffusion matrix operator for elements; $\mathbf{C}^V$ is the system equivalent of $\mathbf{C}^V(q)$. $\mathbf{G}$ is the element–node gradient operator for the system. The nodal gradient operator, $\boldsymbol{\Gamma}$, of (1a) is related to $\mathbf{G}$, by $\boldsymbol{\Gamma} = -[(n^v \mathbf{V}^n)^{-1} \mathbf{Z} \mathbf{V}^e]\mathbf{G}$, where $\mathbf{Z}$ is the $N^n \times N^e$, element-to-node, mapping operator with non-zero entries of unity; $\mathbf{V}^n$ is the diagonal, $N^n \times N^n$ matrix of nodal volumes; $\mathbf{V}^e$ is the diagonal, $N^e \times N^e$, matrix of element volumes and $n^v = 3$ is the number of element vertices. Enforcing the continuity of $\mathbf{u}^e$ ($\mathbf{G}^* \mathbf{u}^e = 0$) where the node–element divergence operator, $\mathbf{G}^*$, is given by $\mathbf{V}^n \mathbf{G}^* = [\mathbf{V}^e \mathbf{G}]^{\mathrm{T}}$ gives the pressure equation (2b) enabling identification of the divergence operator, $\mathbf{C}$, the Poisson-type operator, $\mathbf{B}$, and the source, $\mathbf{s}^p$, i.e.

$$\mathbf{C} = \mathbf{G}^* \mathbf{C}^V \quad \mathbf{B} = \mathbf{G}^* [\mathbf{Q}^e]^{-1} \mathbf{G} \quad \mathbf{s}^p = \mathbf{s}^m - \mathbf{G} [\mathbf{Q}^e]^{-1} \mathbf{s}^e$$

Consider the effects of extreme mesh distortion on these operators. The deformation may be stretching, compaction or combinations of both, but it will be evident from the above analysis that the $\mathbf{u}$–$p$ coupling, $[\mathbf{Q}^e]^{-1}$, will be reduced regardless of how this deformation is implemented. The same is not true of the spatial operators $\mathbf{G}^*$ and $\mathbf{G}$ however where entries in $\mathbf{G}^* \mathbf{G}$ can increase with compaction and reduce with elongation. The combined effects for entries in $\mathbf{B} = \mathbf{G}^* [\mathbf{Q}^e]^{-1} \mathbf{G}$ will depend on both the type of deformation and on the spatial separation of neighbours in relation to the principal axes of the deformation. Nevertheless, it is readily shown that entries $B_{ij}$ will always be preferentially weakened, and hence stability always preferentially compromised between those nodes, $i$ and $j$, separated in the longitudinal direction of stretch (or normal to the direction of compaction). For a unidirectional deformation, we would thus expect to see a unidirectional zebra-stripe pattern of destabilization. Moreover, for lateral compaction, this will be the case even when there has been no change in the longitudinal spacing of nodes.

These findings, and their relevance to the reported problems in Reference [4], will be discussed in the light of numerical experiments in Section 4. Before doing so, the solvers used in Reference [4] are reviewed together with some modifications made.

## 3. SOLVERS AND LINEAR SOLVER MODIFICATIONS

The linear and non-linear equation solvers have been described previously [1–4]. Attention will be focussed on modifications made.

### *3.1. Coupled-variable AMG linear solvers*

*3.1.1. AMG method.* Both linear solvers AMG0 and AMG1 are based on the *unknown* approach [12] in which each grid point represents one degree of freedom. Thus, depending on the number of coupled fields, the grid system can be much larger than the nodal system of the mesh.

AMG0 is based on grid transfer operators of zero order; those for AMG1 approximate first order. As mentioned above, at least first-order operators should strictly be used to ensure a reasonably consistent CGA for an elliptic equation system. To improve the CGA for AMG0 a scaling, $\sigma$, is applied in proportion to the elliptic component of the system [3], where $\sigma = (\beta)^{1/d}$, with $\beta$ the grid coarsening ratio and, $d$, the topological dimension of the grid (here $d = 2$). In the case of AMG1, zero-order transfer operators are smoothed (using an energy optimization

 

procedure) to generate approximately first-order operators that should provide a better CGA. The smoothing is damped (damping factor, $\omega$). Normally, Jacobi smoothing is adopted, $\omega = 2/3$, but heavier damping ($\omega < 2/3$) has also proved useful for highly distorted grids.

*3.1.2. Coarsening algorithms.* The coarsening algorithms for both AMG0 and AMG1 are based on grid-point agglomeration. Grid points are agglomerated if the strength of coupling between them exceeds a certain threshold, defined by a strong coupling parameter, $\varepsilon$, which in Reference [4] was grid dependent. Here it is set at $\varepsilon = 0.08$ regardless of the grid level. Apart from this the aggregation algorithm used is otherwise identical to that given previously for AMG0 [4], but here it is used in both AMG0 and AMG1 solvers.

*3.1.3. Convergence acceleration.* Recognizing that, for both AMG1 and AMG0, there may still be modes of the error spectrum not well represented on the coarse grids, successive iterations are driven with a generalized-conjugate-residual (GCR) control harness. This improves the bandwidth of the correction spectrum and hence the convergence characteristics [3]. Each iteration will be one GCR iteration, and this in turn may consist of one or more multigrid cycles (just one full multigrid V-cycle in all the cases here).

*3.1.4. Solution scheme.* The full multigrid V-cycle (FMV) scheme is a nested recursion of the standard V-cycle scheme, which itself is a recursion of the basic two-level scheme (see Reference [4] for the algorithms used). The two-level scheme involves, the restriction of residual errors from a fine grid to a coarse grid, the efficient determination of broad-bandwidth corrections from these residuals on the coarse grid and the interpolation (prolongation) of those corrections back to the fine grid for an update of the solution. Prior to restriction, a pre-conditioning with $v_1$ sweeps of local relaxation (pre-smoothing) may be used. Following interpolation, high wavenumber errors generated may be reduced with $v_2$ sweeps of post-smoothing. In all the calculations reported here, only post-smoothing is used, $v_1 = 0$; $v_2 > 0$. Note that the smoothing of errors and corrections is not to be confused with the smoothing of transfer operators (for the establishment of the coarse grids).

*3.1.5. Solution smoothing.* Simple Gauss–Seidel (GS) relaxation forms the basis of the smoothing algorithm. As multiple Gauss–Seidel relaxation sweeps will not be stable for the system matrix of Equations (2), some form of stabilization is required. A GCR control harness provides this. It will be referred to as GS smoothing, the stabilization being understood.

*3.1.6. Solution smoothing sequence.* In the previously reported work [4] (but not in Reference [1]) field equations were visited somewhat randomly during smoothing. This had a deleterious effect on performance and is partly responsible for some of the reported convergence failures. It has been rectified in the current scheme where an ordering is imposed on the visiting sequence. Firstly, there is an ordering according to the field identity of the equations; flow vector components are visited first, each separately, whilst the pressure equation set is visited last, as in Reference [1]. Secondly, an option for subset ordering is introduced. In the case of AMG1, the subsets are those fine grid points associated with a particular coarse grid point. In the case of AMG0, the core of a subset consists those points that are agglomerated into a coarse grid point and to these are added the immediately adjacent fine-grid points. These subsets are visited in order of their field identity as just described, all points within a

 

subset are visited before moving on to the next (the method comes under the classification of Box–Gauss–Seidel (BGS) schemes [13]).

*3.1.7. Solution smoothing regime.* The number of post-smoothing sweeps employed is chosen to meet the demands of the problem being addressed. This was also the strategy used in the previous work [4]. Here, an option to vary the number of smoothing sweeps with the grid level has been introduced. For example, the number of sweeps for grid level, $g$, will be $v_2 = vg$, where $v$ is the number of post-smoothing sweeps on the finest grid. $g$ will range from 1 to $N_g - 1$, where $N_g$ is the total number of grids (a direct solver is always used on the coarsest grid).

*3.1.8. CGA complexity.* Another way of driving the AMG0 solver 'harder' is to increase the complexity of the CGA by increasing $\beta$. Complexity is defined in terms of two numbers, grid complexity, $C_g$, and algebraic complexity, $C_A$. $C_g$ is the ratio of the total number of equations over all grids to the number of equations on the fine grid. Likewise, $C_A$ is the ratio of the total number of matrix entries over all grids to the number for the fine grid. In the case of AMG0, $C_A \approx C_g$, whereas in the case of AMG1, $C_A > C_g$ due to the increased bandwidth brought about by smoothing the inter-grid transfer operators. There is little scope for increasing $C_g$ in the case of AMG1; it is constrained by the need for a sufficiently large core of points in each aggregate (i.e. sufficiently small $\beta$) to provide a meaningful, multi-dimensional, linear interpolation. Increasing $C_g$ is therefore only considered an option for AMG0 ($\beta \leqslant 0.5$; $C_g \approx C_A \leqslant 2$).

## 4. NUMERICAL EXPERIMENTS

### 4.1. Test problems

Attention is focussed on lamina pressure-driven flow in a rectangular channel. This is a simple problem with an easy analytic solution but which, nonetheless, proved difficult for the AMG0/AMG1 solvers when cast as a discrete problem on highly stretched grids. It is therefore appropriate for this investigation and has the advantage of giving estimates for the true errors.

The length-to-half-width ratio is 16. A solid, no-slip wall and a free slip symmetry axis constitute the top and bottom boundaries, respectively. The left and right, inlet and outlet, are fixed pressure boundaries. Discrete approximations are all of similar size (between 32 768 and 36 864 elements) regardless of the mesh anisotropy. On uniform meshes, therefore, elements all have the same volume, being longitudinally stretched and laterally compacted to achieve the required range of aspect ratio. On non-uniform meshes, the lateral compaction is graded across the channel (low aspect ratios along the axis, high aspect ratios along the wall). Element volumes therefore vary across the domain in these cases, decreasing towards the wall but the total number of elements is kept within the range 32 768–35 880.

The first set of test cases considered is that of uniform anisotropic meshes for aspect ratios in the range $\alpha = 1$ to 256, corresponding to grids from $512 \times 32$ to $32 \times 512$.

All calculations are for one Reynolds number, $Re = 0.125$, based on hydraulic diameter for channel flow.

 

### 4.2. The assessment of solver performance

*4.2.1. Solver convergence.* Since the problem is essentially linear (unidirectional lamina flow) there is no distinction between Navier–Stokes convergence and linear solver convergence. A 12-order reduction in the Euclidian norm of corrections is set as a convergence target. Normally, such a tight tolerance level would be extravagant. It is adopted here simply to monitor performance over the entire range of possible convergence, thus ensuring that a stalled convergence (due to potentially unstable discretizations) could not pass undetected.

*4.2.2. Linear solver performance.* Overall performance of the linear solver will be assessed in terms of average reduction factors. The average reduction factor, $\rho$, for a total of $n_f$ FMV cycles and $n_i$ non-linear iterations is taken to be

$$\rho = \frac{1}{n_i}\sum_{n=1}^{n_i}\rho^n \quad \text{where} \quad \rho^n = \left\{\prod_{f=1}^{n_f}\rho^{(f,n)}\right\}^{1/n_f} \quad \text{and} \quad \rho^{(f,n)} = \frac{\|\mathbf{r}^{(f,n)}\|_2}{\|\mathbf{r}^{(f-1,n)}\|_2}$$

with $\mathbf{r}(f,n)$ being the residual following the $f$th FMV cycle during the $n$th Picard iteration. Convergence failure is here taken to be stagnated convergence ($\rho^n \to 1$).

### 4.3. Numerical results

*4.3.1. AMG1 reduction factors: uniform anisotropic meshes.* In Figure 4(a) the average reduction factors, $\rho$, for AMG1 are plotted for aspect ratios, $\alpha$, up to 256. Consider first points without a numeral sub/superscript (filled circles), which were obtained with just three

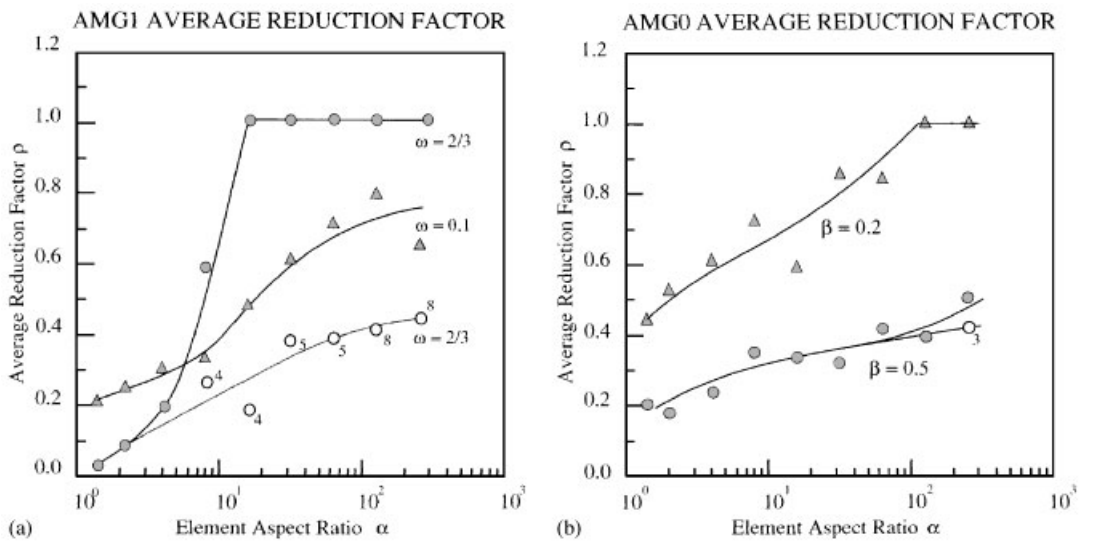


Figure 4. (a) AMG1: averaged, residual-reduction factors for channel flow ($Re = 0.125$) discretized on uniformly anisotropic meshes; and (b) AMG0: averaged, residual-reduction factors for channel flow ($Re = 0.125$) discretized on uniformly anisotropic meshes.

 

post-smoothing sweeps for all grids. It will be evident that, with Jacobi-smoothed transfer operators, the reduction factors for AMG1 ($\omega = 2/3$; $v_2 = 3$) deteriorate rapidly as the aspect ratio increases and that for aspect ratios greater than 8, stagnation occurs. Note however that convergence can be achieved with a heavier damping of the transfer-operator smoothing, AMG1 ($\omega = 0.1$, $v_2 = 3$), though the reduction factors are relatively poor at the higher anisotropy (filled triangles). Better performance (open circles) is achieved by retaining the Jacobi smoothing of transfer operators and increasing the solution smoothing on the coarse grids, AMG1 ($\omega = 2/3$, $v_2 = vg$). This requirement for a larger investment in solution smoothing is consistent with the findings of the previous work, although in that work a larger investment was required (strict ordering according to field identity in the smoothing sequence is responsible for the improvement).

*4.3.2. AMG1 pressure errors: uniform anisotropic meshes.* For the test problem, the pressure solution should be linear between the prescribed inlet and outlet. It will be instructive therefore to examine how the above convergence, or lack of convergence, is reflected in the relative error in pressure along the axis of the channel.

Figures 5(a) and (b) show the relative error, $\Delta p(x)/p_t(0)$, in the calculated pressure, $p(n)$, compared with the theoretical pressure, $p_t(x)$, where

$$\frac{\Delta p(x)}{p_t(0)} = \frac{p(n) - p_t(x)}{p_t(x=0)}$$

This is plotted against distance, $x$, along the axis of the channel for the first five iterations of the two most extreme cases of Figure 4(a) (i.e. cases $v_2 = 3$, $\alpha = 256$ and $v_2 = 8g$, $\alpha = 256$). The initial error follows the single linear profile for non-boundary nodes marked ITER = 0 (the initial pressure field for free nodes was zero).

Consider first Figure 5(a), results for AMG1 ($\omega = 2/3$, $v_2 = 3$). From the first iteration onwards, it will be evident that there is indeed a splitting into two pressure solutions, as suggested by the analysis of Section 2; they are the upper and lower bounds of the 'wiggles' drawn as a zigzag line. The upper bound represents the odd-row pressure sub-system, containing the boundary nodes; the lower bound represents the even-row sub-system that is only weakly coupled (via the odd-row sub-system) to the boundary nodes.

The odd-row sub-system shows a reduction in all components of the error spectrum over the first four iterations. Thereafter the reductions tend to stall. There are some reductions beyond the 5th iteration (not shown); but beyond about the 10th iteration the convergence has completely stalled.

The even-row sub-system shows no evidence of convergent behaviour beyond the first iteration. The error lies mainly in the low- and zero-wavenumber components of the spectrum, giving a large offset along the channel axis, 'a constant of the integration'.

There was no evidence of any transverse oscillations within either sub-system that would be consistent with a checker-board pattern of instability. If any existed, it was undetectable on the background noise of the error spectrum. The amplitude of the noise was less than 7% of the mean relative error across the channel (0.65% of the mean pressure) and the high-wavenumber component of this was smaller by at least one order. The instability has therefore the zebra-stripe pattern discussed in Section 2.

Clearly, for AMG1, just three post-smoothing sweeps fail to have any impact in reducing the low-wavenumber components of the error spectrum for the weakly coupled even-row

 

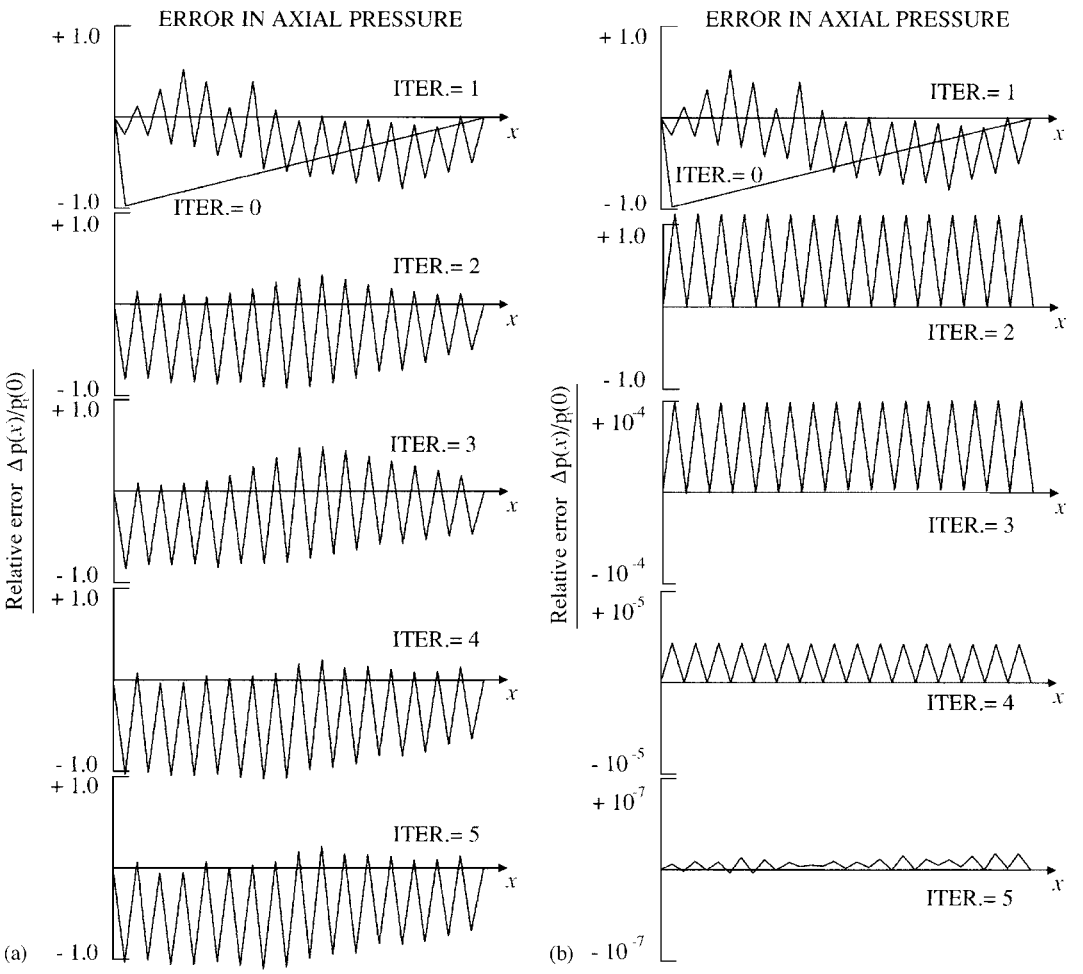


Figure 5. (a) AMG1 ($\omega = 2/3$, $v_2 = 3$) solver. Relative error in axial pressure profile for channel flow $Re = 0.125$; mesh aspect ratio $\alpha = 256$; BGS post-smoothing; and (b) AMG1 ($\omega = 2/3$, $v_2 = 8g$) solver. Relative error in axial pressure profile for channel flow $Re = 0.125$; mesh aspect ratio $\alpha = 256$; BGS post-smoothing.

sub-system, and the progress for the odd-row system is stalled. However, by driving the solver harder for the second and subsequent iterations, using additional smoother sweeps on the coarser grids (see Section 2.3.7), there is an abrupt change to convergent behaviour (Figure 5(b)). On the first iteration, just three smoothing sweeps are employed so Figures 5(a) and (b) are identical. For the second and subsequent iterations, $v_2 = 8g$ sweeps are applied. Observe that by the 2nd iteration there is no visible amplitude modulation of the 'wiggles', indicating that, with the exception of the zero-wavenumber component of error for the even-row sub-system, there has been a large reduction in all components of the error spectra. The even-row, zero-wavenumber component has actually increased slightly to give a large,

 

constant-amplitude 'wiggle' along the channel. Note however that by the 3rd and for subsequent iterations this component is also reduced significantly (note changes in scale from iteration to iteration). By the 5th iteration, the two sub-systems have errors that agree to within $2 \times 10^{-8}$ of each other; any difference is of the same order as the variations within each solution separately. This level of the real relative error compares with a reduction of $10^{-13}$ in the residual norm for this particular calculation.

It is concluded that the AMG1 ($\omega = 2/3,\ v_2 = 8g$) can bring both the weakly coupled and the strongly coupled sub-systems to a common convergence. The stagnated convergence for AMG1 ($\omega = 2/3,\ v_2 = 3$) is characterized by a failure to reduce the low/zero-wavenumber components of the error in the weakly coupled, even-row, sub-system.

*4.3.3. AMG0 reduction factors: uniform anisotropic meshes.* For the AMG0 solver two values for the grid coarsening ratio, $\beta$, are used, $\beta = 0.2$ ($C_g$ and $C_A \sim 1.5$) and $\beta = 0.5$ ($C_g$ and $C_A \sim 2$). Values lower than 0.2 resulted in convergence failure. Convergence factors for the two cases are plotted against element aspect ratio in Figure 4(b).

For $\beta = 0.2$, with just three smoothing sweeps on each grid, convergence is obtained in most cases. Admittedly reduction factors are not particularly good, but they are convergent. Breakdown occurs for aspect ratios in excess of 64.

For $\beta = 0.5$, convergence is better, and robust for $\alpha \leqslant 256$. The reduction rate at the largest aspect ratio may be just showing some evidence of weakening, but the difference between the $\rho(v_2 = 3)$ rate and the $\rho(v_2 = 3g)$ rate is small (note that the robustness of this AMG0 ($\beta = 0.5,\ v_2 = 3$) performance is eroded if the above-mentioned strict ordering according to field identity in the smoothing sequence is not respected).

*4.3.4. AMG0 pressure errors: uniform anisotropic meshes.* Clearly, AMG0 ($\beta = 0.5,\ v_2 = 3$) performs better than AMG1 ($\omega = 2/3,\ v_2 = 3$) for the highly anisotropic discretizations. Examine therefore how this better performance is reflected in the reduction of errors in the axial pressure distribution.

Consider first the results for AMG0 ($\beta = 0.5,\ v_2 = 3$), Figure 6(a). All components of the error spectrum are reduced together, including the zero-wavenumber component (note again changes in scale from iteration to iteration). The zero-wavenumber component for the even-row sub-system does lag behind that of the odd-row sub-system slightly, so there are wiggles, but by the 4th iteration both sub-systems are close to convergence. AMG0 ($\beta = 0.5,\ v_2 = 3$) is thus efficient in reducing all spectral components of the pressure error for both sub-systems.

Increasing the smoothing (Figure 6(b)) does not improve performance; if anything, it is slightly worse insofar as the error for the even-row sub-system is still larger than that for odd-row sub-system at the 4th iteration. However, by the 5th iteration, convergence is reached; the error profile is then the same as those in Figure 6(a), AMG0 ($\beta = 0.5,\ v_2 = 3$), and Figure 5(b), AMG1 ($\omega = 2/3,\ v_2 = 8g$), despite the different paths followed in each case.

*4.3.5. Comparison of AMG1 and AMG0 convergence: uniformly anisotropic meshes.* Compare now AMG1 and AMG0 reduction factors over the full range of anisotropy (Figures 4(a) and (b)). For the more stable problems, of low-to-moderate aspect ratio, AMG1 ($\omega = 2/3,\ v_2 = 3$) reduction factors are significantly better than those for AMG0 ($\beta = 0.5,\ v_2 = 3$). Here, as would be expected, the smoothed, inter-grid, transfer operators are effective in improving

 

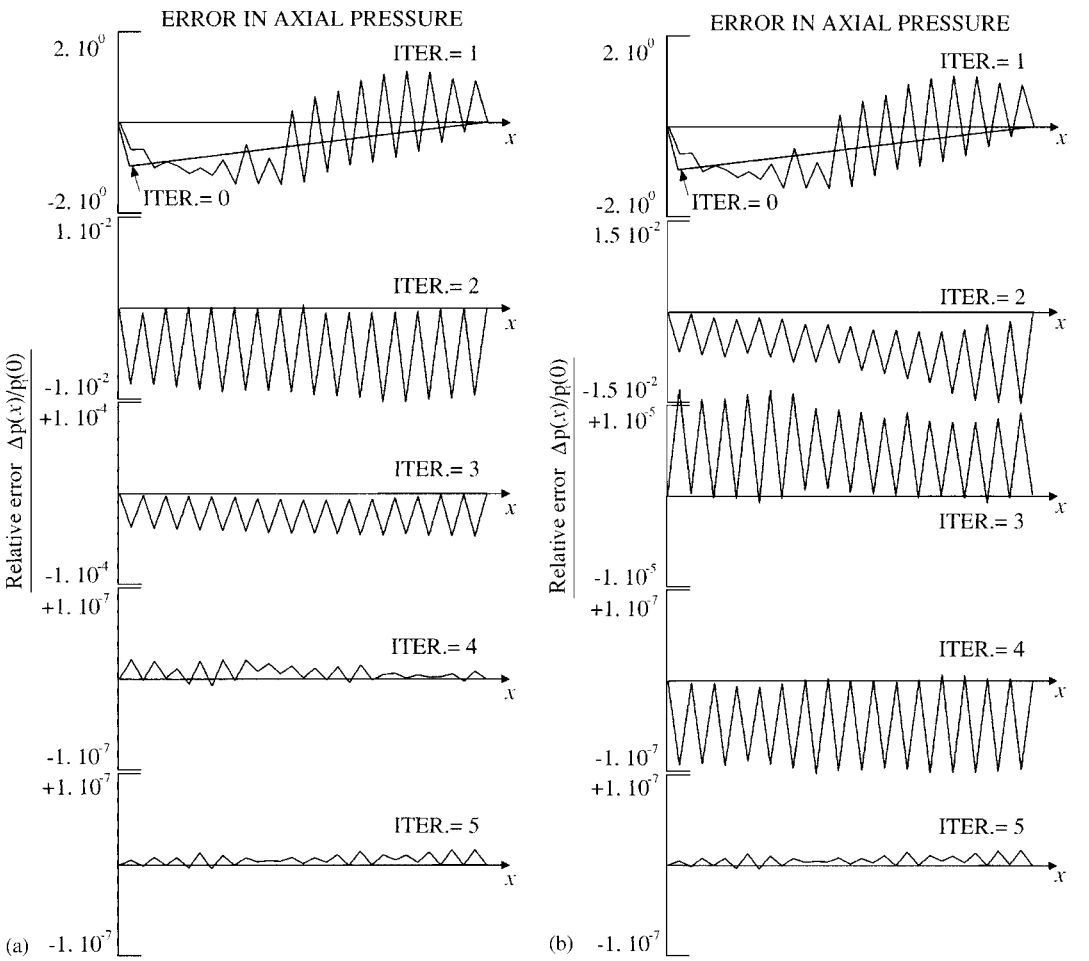


Figure 6. (a) AMG0 ($\beta = 0.5$, $v_2 = 3$) solver. Relative error in axial pressure profile for channel flow $Re = 0.125$; mesh aspect ratio $\alpha = 256$; BGS post-smoothing; and (b) AMG0 ($\beta = 0.5$, $v_2 = 3g$) solver. Relative error in axial pressure profile for channel flow $Re = 0.125$; mesh aspect ratio $\alpha = 256$; BGS post-smoothing.

the CGA. For the problems of high anisotropy, on the other hand, the reduction factors for AMG1 ($\omega = 2/3$, $v_2 = 8g$) are no better than those for AMG0 ($\omega = 0.5$, $v_2 = 3$), if anything slightly worse, and of course those for AMG1 ($\omega = 2/3$, $v_2 = 3$) are not convergent at all. This suggests that the transfer-operator smoothing is less effective for highly stretched grids.

For high anisotropy, it would appear that AMG0 (with sufficient complexity) offers a more robust performance than does AMG1.

*4.3.6. AMG1 relative pressure errors: non-uniform anisotropic meshes.* According to Section 2, the decoupling of the odd and the even rows occurs because the entire calculational

 

domain is covered by elements of high aspect ratio. If part of the calculational domain were spanned by more isotropic elements, then this should provide the necessary coupling between the two sub-systems that would inhibit destabilization. The even-row sub-system would be in better contact with the boundary conditions and the problem better defined. Thus, for example, a single line of more isotropically coupled, non-boundary, nodes spanning the channel longitudinally, should 'zip' the two systems together, enhancing stability and convergence, despite the fact that most of the domain remains uniformly covered with elements of very high aspect ratio.

*Mesh with a discontinuous change in anisotropy.* To test this argument, a single line of such nodes (less than 0.26% of the total) was laid down just inside the axial boundary, using elements of aspect ratio $\alpha = 4$. All remaining elements had aspect ratio $\alpha = 256$, so the average aspect ratio (253.4) was very close to the maximum. Good convergence was indeed achieved for AMG1 ($\omega = 2/3,\ v_2 = 3$) in this case (Figure 7(a)), precisely the case which failed previously; compare with Figure 5(a). The difference between odd-row and even-row sub-systems is damped significantly, being now much smaller than the mean error in each separately, which is reduced rapidly by about seven orders in four iterations. This final level of mean error is not as low as that for the original meshes because the mesh is now coarser near the axis.

*Mesh with a graded change in anisotropy*. Of course a 2-order step change in mesh size would be avoided in practice in favour of smoothly graded changes. Figure 7(b) shows AMG1 ($\omega = 2/3,\ v_2 = 3$) results for such a mesh with a smooth grading from $\alpha = 4$ on the axis to $\alpha = 256$ at the wall, average aspect ratio of 130. As the number of transverse nodal intervals was reduced in the grading process, the axial resolution has been doubled to maintain problem size, hence the higher wavenumber components in the error. These are smaller than those in Figure 7(a) and the convergence is improved slightly.

*4.3.7. Comparison of AMG1 and AMG0 reduction factors: graded anisotropic meshes.* Similarly, good convergence was achieved for graded meshes right across the range of maximum aspect ratio up to 256 (Figures 8(a) and (b)), which may be compared directly with Figures 4(a) and (b). Note again, that at high aspect ratio, the convergence factors for AMG1 ($\omega = 2/3,\ v_2 = 3$) are no better than those for AMG0 ($\beta = 0.5,\ v_2 = 3$), whereas at moderate to low aspect ratio they are significantly better. This is consistent with the above observations for uniformly anisotropic meshes and again suggests that transfer-operator smoothing is less effective in improving the CGA for highly anisotropic meshes.

### *4.4. Summary of principal observations and their interpretation*

#### *4.4.1. For uniform anisotropic meshes.*

1. Convergence performance deteriorates with increasing anisotropy.
2. The deterioration is solver dependent and worst for AMG1 ($\omega = 2/3,\ v_2 = 3$), to the point of stagnation for aspect ratios greater than 8.
3. The convergence difficulties are accompanied by a bifurcation of the pressure system and an associated zebra-stripe pattern of instability in the pressure field.
4. Stagnated convergence is characterized by an inability to reduce the low/zero-wavenumber components of the pressure error for the more weakly coupled of the two pressure sub-systems.

 

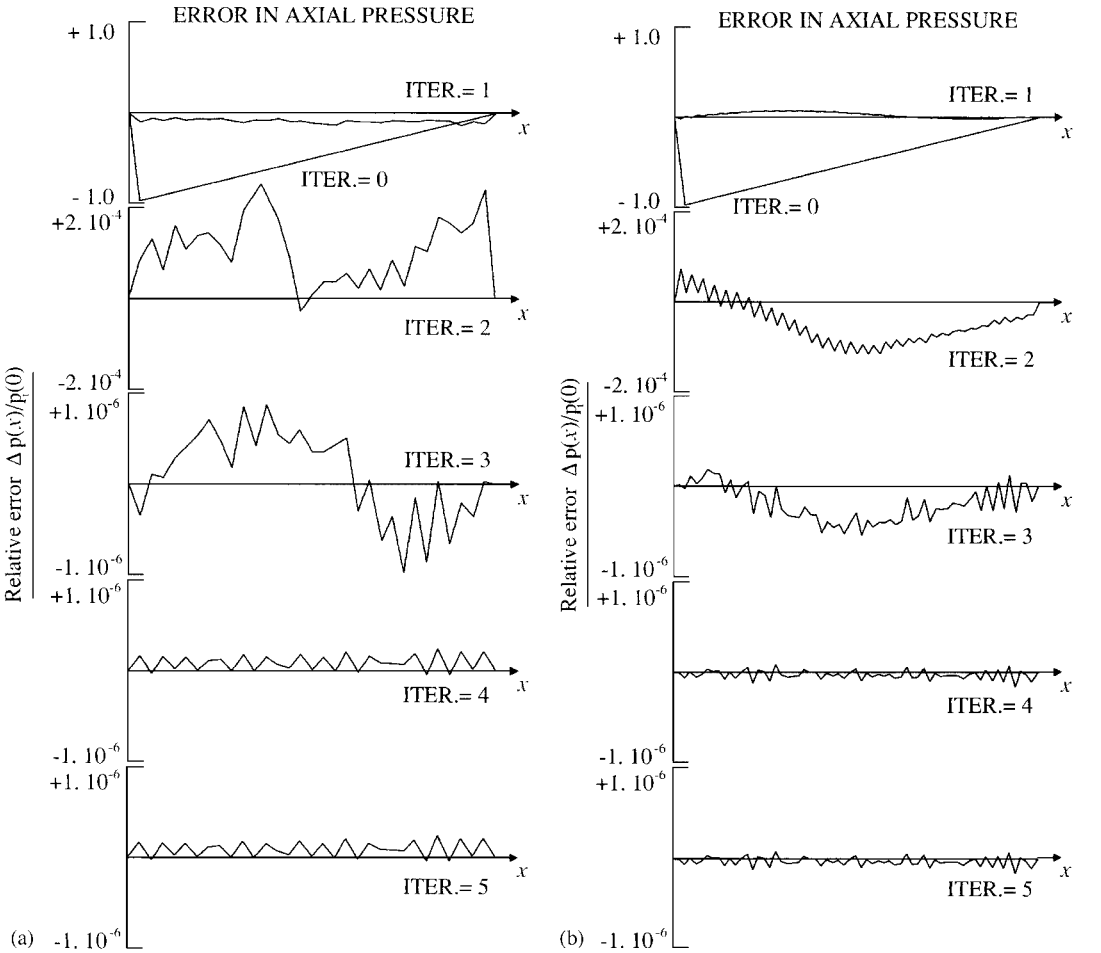


Figure 7. (a) Mesh with step change in anisotropy ($\alpha_{\min} = 4$; $\bar{\alpha} = 253.4$; $\alpha_{\max} = 256$). Relative error in axial pressure for channel flow; $Re = 0.125$. AMG1 ($\omega = 2/3$, $v_2 = 3$) solver; BGS post-smoothing; and (b) mesh with graded change in anisotropy ($\alpha_{\min} = 4$; $\bar{\alpha} = 130$, $\alpha_{\max} = 256$). Relative error in axial pressure for channel flow; $Re = 0.125$. AMG1 ($\omega = 2/3$, $v_2 = 3$) solver; BGS post-smoothing.

*4.4.2. For non-uniform anisotropic meshes.*

1. The zebra-stripe patterns of instability are less evident: differences between the two subsystems are small compared to the levels of the relative error in both.
2. AMG0 ($\beta = 0.5$, $v_2 = 3$) convergence rates are independent of mesh anisotropy.
3. AMG1 ($\omega = 2/3$, $v_2 = 3$) convergence rates show some deterioration with increased anisotropy; reduction factors degrade from levels much better than AMG0 to levels comparable with those of AMG0 (Figures 8(a) and (b)). This is unlikely to be associated with any destabilization of the discretization (Point 1 above). It is more likely to be due to an erosion of the quality of the smoothed transfer operators for highly anisotropic grids.

 

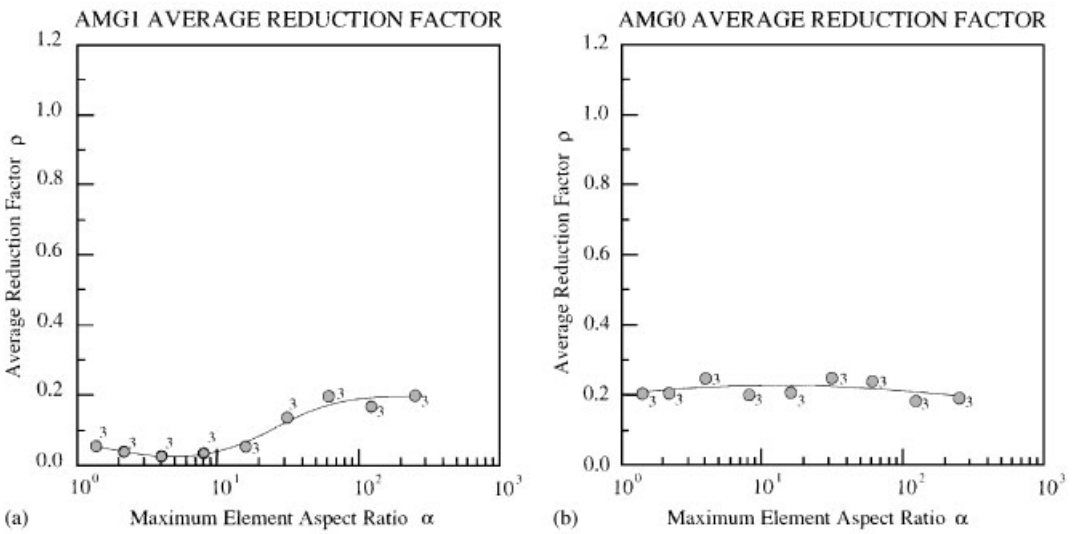


Figure 8. (a) AMG1 ($\omega = 2/3$, $v_2 = 3$): averaged residual-reduction factors for channel flow ($Re = 0.125$) discretized on non-uniform, anisotropic, meshes; and (b) AMG0 ($\beta = 0.5$, $v_2 = 3$): averaged, residual-reduction factors for channel flow ($Re = 0.125$) discretized on non-uniform, anisotropic, meshes.

These observations are in qualitative agreement with the predictions made on the basis of the analysis of Section 2, and as such offer strong evidence for a causal link between the destabilization of discretizations on anisotropic meshes and the observed poor performance of both solvers.

## 5. DISCUSSION

The weakening of the velocity–pressure coupling is a direct result of the large diffusion coefficient for high-aspect-ratio elements, due to the large transverse areas for the lateral diffusion of momentum. The problem could arise, therefore, in all discretizations for collocated meshes that rely on the so-called 'momentum interpolation' approach for the provision of velocity–pressure coupling. These could include, the Rhie and Chow scheme and the various forms of CPI schemes, such as the one used here. Convergence difficulties with a cell-centred, Rhie and Chow method for flows on highly stretched grids have been observed (see introductory remarks in Reference [14]), though it is not clear if the type of instability being discussed here is implicated.

For the cell-centred, collocated CPI scheme of Deng *et al.* [11], the transverse diffusion of momentum is not treated implicitly in element interpolation. Only the longitudinal component is implicit. Consequently, the transverse component does not contribute to the diffusion coefficient of the element, $D$, and therefore does not weaken the velocity–pressure coupling, $[\mathbf{Q}^e]^{-1}$. The scheme should thus be stable. Since, however, the transverse diffusion is treated

 

explicitly as a function of nodal velocities only, the penalty will be very large positive and negative entries in the off-diagonal block, **C**, of the pressure equation. These will be larger than the other entries in that block (and the diagonal block) by a factor $\sim\alpha^2$ , and this could lead to other convergence difficulties.

In most practical applications, highly stretched/compacted elements are usually exploited in an attempt to achieve an economic, directional, refinement (for example to resolve boundary layers near a wall). As such there is no real need to have a blanket deployment of such elements over the entire domain. In view of this (and bearing in mind results for non-uniform meshes) the type of decoupling being discussed is an avoidable problem and may therefore be considered somewhat academic. Nevertheless, as the method is used in many commercial codes it is a limitation of which all practitioners should be aware.

## 6. CONCLUSIONS

The velocity–pressure coupling that is implicit in physical interpolation schemes, and is essential for the stability of Navier–Stokes discretizations on collocated meshes, can be degraded on severely stretched/compacted meshes.

This weakens the nodal coupling between nearest neighbours of the pressure system along the direction of stretch (normal to the direction of compaction) allowing a destabilizing bifurcation into alternate, transverse, rows of next-nearest neighbour nodes, an odd-row sub-system and an even-row sub-system. Differences between them are manifest as a zebra-stripe pattern of spatial instability, with longitudinal oscillations (wiggles) in pressure.

Imposed boundary conditions may be divided between the sub-systems or, totally excluded from one of them, so the problem will not be well defined and convergence difficulties can arise.

Such a destabilization is consistent with the reported poor performance of algebraic multigrid solvers when applied to Navier–Stokes problems discretized on highly anisotropic meshes, which at least in part, was wrongly attributed to deficiencies in the solvers.

The problem is inherent in the equations and will not be addressed by improving solvers.

Some solvers may, however, be more tolerant of the problem than others. For example, the solver AMG0 ($\beta = 0.5$, $v_2 = 3$) is more tolerant than AMG1 ($\omega = 2/3$, $v_2 = 3$) for the test problem investigated.

The problem can be alleviated by employing a graded mesh, so that the elements of more moderate aspect ratio improve the coupling.

This type of instability could occur in other discretizations for collocated meshes.

## REFERENCES

1. Webster R. An algebraic multigrid solver for Navier Stokes problems. *International Journal for Numerical Methods in Fluids* 1994; **18**:761–780.
2. Webster R. An algebraic multigrid solver for Navier Stokes problems in the discrete second-order approximation. *International Journal for Numerical Methods in Fluids* 1996; **22**:1103–1123.
3. Webster R. Efficient algebraic multigrid solvers with elementary restriction and prolongation. *International Journal for Numerical Methods in Fluids* 1998; **28**:317–336.
4. Webster R. Performance of algebraic multigrid solvers based on unsmoothed and smoothed aggregation. *International Journal for Numerical Methods in Fluids* 2001; **36**:743–772.
5. Brandt A, Dinar N. Multigrid solutions to flow problems. In *Numerical Methods for Partial Differential Equations*, Parter S (ed.). Academic Press: New York, 1979; 53–147.

 

6. Patankar SV. *Numerical Heat Transfer and Fluid Flow*. Hemisphere: Washington, DC, 1980.
7. Rhie CM, Chow WL. Numerical study of the turbulent flow past an airfoil with trailing edge separation. *AIAA Journal* 1983; 1525–1532.
8. Prakash C. An improved control-volume finite-element method for heat and mass transfer and for fluid flow using equal order velocity–pressure interpolation. *Numerical Heat Transfer* 1986; **9**:253–276.
9. Hookey NA. Evaluation and enhancements of control-volume finite-element methods for two-dimensional fluid flow and heat transfer. *M.Eng. Thesis*, Department of Mechanical Engineering, McGill University, Montreal, 1986.
10. Schneider GE, Raw MJ. Control volume finite-element method for heat transfer and fluid flow using collocated variables. *Numerical Heat Transfer* 1987; **11**:363–390.
11. Deng GB, Piquet J, Queutey P, Visonneau M. Incompressible flow calculations with a consistent physical interpolation finite volume approach. *Computers and Fluids* 1994; **23**(8):1029–1047.
12. Ruge J, Stüben K. Algebraic multigrid. In *Multigrid Methods*, vol. 5, Cormick S (ed.). Frontiers in Applied Mathematics. SIAM: Philadelphia, 1987.
13. Brandt A. General highly accurate algebraic coarsening. *Electronic Transactions on Numerical Analysis*, vol. 10. 2000; 1–20.
14. Deng GB, Piquet J, Vasseur X, Visonneaux M. A new fully coupled method for computing turbulent flows. *Computers and Fluids* 2001; **30**:445–472.

 